Cell, Vol. 100, 537–549, March 3, 2000, Copyright ©2000 by Cell Press

Solution Structure of the *E. coli* 70S Ribosome at 11.5 Å Resolution

Irene S. Gabashvili,[†] Rajendra K. Agrawal,[†‡] Christian M. T. Spahn,[*†] Robert A. Grassucci,[*†] Dmitri I. Svergun,[§‖] Joachim Frank,[*†‡#] and Pawel Penczek[†‡]

[*]Howard Hughes Medical Institute
Health Research, Inc.
[†]Wadsworth Center
Empire State Plaza
Albany, New York 12201-0509
[‡]Department of Biomedical Sciences
State University of New York at Albany
Empire State Plaza
Albany, New York 12201-0509
[§]European Molecular Biology Laboratory
c/o DESY
Notkestraße 85
D-22603 Hamburg
Germany
[‖]Institute of Crystallography
Russian Academy of Sciences
Leninsky pr. 59
117333 Moscow
Russia

Summary

Over 73,000 projections of the *E. coli* ribosome bound with formyl-methionyl initiator $tRNA_f^{Met}$ were used to obtain an 11.5 Å cryo-electron microscopy map of the complex. This map allows identification of RNA helices, peripheral proteins, and intersubunit bridges. Comparison of double-stranded RNA regions and positions of proteins identified in both cryo-EM and X-ray maps indicates good overall agreement but points to rearrangements of ribosomal components required for the subunit association. Fitting of known components of the 50S stalk base region into the map defines the architecture of the GTPase-associated center and reveals a major change in the orientation of the α-sarcin-ricin loop. Analysis of the bridging connections between the subunits provides insight into the dynamic signaling mechanism between the ribosomal subunits.

Introduction

The *Escherichia coli* 70S ribosome is a complex macromolecular assembly that consists of three rRNA molecules and over 50 proteins. To date, cryo-electron microscopy (cryo-EM) has been the only viable approach to the study of its structure (Frank et al., 1995b; Stark et al., 1995; Malhotra et al., 1998). The importance of cryo-EM studies lies in the fact that they allow ribosomes to be readily visualized in many different functional states without the need for crystallization (Agrawal et al., 1996, 1998, 1999a, 1999c; Stark et al., 1997a, 1997b).

Crystals suitable for X-ray crystallographic studies have been obtained only for ribosomes of organisms living in extreme environments (i.e., halophilic archeon: Ban et al., 1998, 1999; and thermophilic bacteria: Cate et al., 1999; Clemons et al., 1999; Harms et al., 1999; Schlünzen et al., 1999). Comparison of structures resulting from these studies, now in the resolution range of 5–8 Å, with those of mesophilic *E. coli* will be extremely useful in shining light on the process of molecular adaptation. At the same time, comparison between X-ray and cryo-EM maps helps in identifying flexible domains that are distorted on account of the packing in the crystal (Penczek et al., 1999). The best-defined 3D motifs, of double-stranded A form rRNA, are 17–20 Å in diameter with major grooves that can reach 13.5 Å in depth. Thus, resolutions in the 13 to 10 Å range are sufficient for detection and interpretation of such structural features and elements richly presented on the surface and at the subunit interface (Ban et al., 1999; Cate et al., 1999; Clemons et al., 1999).

Here, we present an 11.5 Å cryo-EM map of the *E. coli* 70S ribosome initiation-like complex with fMet-$tRNA_f^{Met}$ at the P site. Guided by recent placements of proteins and rRNA elements in X-ray maps, we were able to identify some of the ribosomal components and the nature of connections between the ribosomal subunits. The map also elucidates the architecture of functionally important domains. Structural details seen at this resolution, especially when put into the context of cryo-EM mappings of EF-G (Agrawal et al., 1998, 1999a, 2000), begin to reveal the identity and functional interplay of the connections between the regions associated with decoding, peptidyl transfer, and GTPase activity.

Results

Cryo-Electron Microscopy and Three-Dimensional Reconstruction

The cryo-EM density map was obtained from a total of 73,523 projections of the fMet-$tRNA_f^{Met}$·ribosome complex in a defocus range of 0.73 to 4.34 μm (see Experimental Procedures). The Fourier shell correlation curve (Figure 1) of the final, contrast-transfer function-corrected reconstruction indicates a resolution of 11.5 Å for a 0.5 cutoff (Böttcher et al., 1998). Although some useful information extends to 8.4 Å (3 σ criterion; Orlova et al., 1997), its inclusion into the final map is not justified as the signal-to-noise ratio falls below 1 (Malhotra et al., 1998). In the reconstruction, Fourier amplitudes at higher spatial frequencies are always underrepresented due to charging, instrument instabilities, specimen drift, and partial coherence. To compensate for these effects, we obtained scattering intensities using X-ray solution scattering measurements for *E. coli* ribosomes in the range up to 1/8 $Å^{-1}$, and applied a correction to the Fourier amplitudes up to the 1/11.5 $Å^{-1}$ cutoff point (Figure 1). The correction corresponds approximately to

#To whom correspondence should be addressed (e-mail: joachim@wadsworth.org).

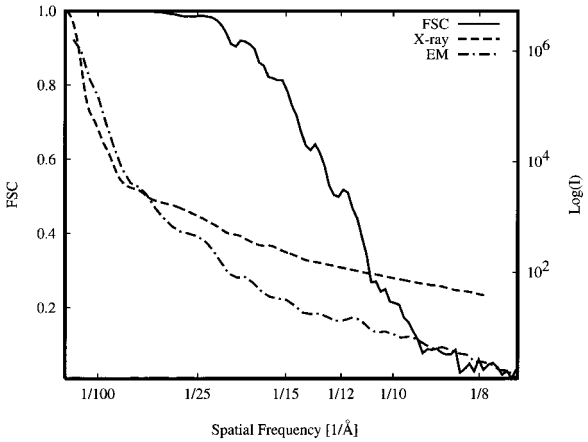

Figure 1. Assessment of Resolution, and Basis for Fourier Amplitude Correction

The Fourier shell correlation (FSC) curve (solid line) falls below 0.5 at 11.5 Å. Averaged radial falloff of Fourier intensities obtained from cryo-EM reconstruction (dashed/dotted line) versus measured using low-angle solution scattering of *E. coli* ribosomes (dashed line). The ratio of the two latter curves was used as a basis for correcting the EM Fourier amplitudes to obtain the final density map.

a temperature factor with B = -310 Å^2 (definition as in Glaeser and Downing, 1992). Application of this relatively small factor is justified in the range of spatial frequencies where the Fourier transform is statistically well defined.

For surface representations, threshold values were selected using the molecular volume as a guide. The protein level was initially chosen to encompass the total volume of 2.6×10^6 Å^3, based on the chemical molecular weight (Wittmann et al., 1982). We used a slightly enlarged volume of 2.68×10^6 Å^3 to retain continuity of some structural features. The RNA level was chosen to yield a protein/RNA ratio of 0.72:1.0. Around this threshold level, the appearance of the strands changed little when the level was varied.

Structure of Initiator-tRNA

The quality of a 3D cryo-EM reconstruction can be assessed when a component can be identified that is known at atomic resolution, by comparing its appearance with that of a low-resolution map computed from atomic coordinates. For comparison with the tRNA portion of the cryo-EM map, we used the X-ray coordinates of the yeast initiator tRNA (Basavappa and Sigler, 1991) and *E. coli* fMet-tRNA$_f^{Met}$ interacting with the methionyl initiator tRNA$_f^{Met}$ transformylase (Schmitt et al., 1998; inset in Figure 2, right). The structure corresponding to fMet-tRNA$_f^{Met}$ reveals details expected at 10 Å resolution (inset in Figure 2, left), proving the reliability of the other fine structural detail observed in the density map (Figure 2). Moreover, the overall shape and geometry of the tRNA in the cryo-EM map show specific structural features of *E. coli* fMet-tRNA$_f^{Met}$ (Schmitt et al., 1998), as opposed to the initiator tRNA of yeast. The acceptor and anticodon ends of the tRNA are seen as spirally distributed densities with distinguishable major and minor grooves. Both T and D loops are readily recognized. Connections of the tRNA with the 70S ribosome observed earlier (Malhotra et al., 1998) have become much more distinct.

Secondary-Structure Elements Visible in the Cryo-EM Map

The 3D map of the *E. coli* 70S ribosome at 11.5 Å resolution (Figure 2) shows numerous strands of relatively high densities with well-defined geometry such as right-handed twists and deep grooves characteristic of the A form conformation of rRNA. At this level of resolution it is not possible to unambiguously differentiate between RNA and proteins or to identify their recognition and binding determinants. Some of the helices, interpretable as rRNA, appear relatively isolated in the ribosome and run a long way before merging with other ribosomal secondary structure elements. A number of such structures are located between the ribosomal subunits, strongly resembling the corresponding elements of the crystallographic maps at ~8–5 Å.

30S Subunit

The interface side of the 30S subunit mainly consists of high-density material. Separate helical strands form the frames of body and shoulder (Figures 2a–2c) and define the skeleton of the platform (Figure 3, bottom). Helical elements also form the spur and two other strands intersecting with it at the bottom of the subunit (Figures 2b–2d). Separate strands connecting the head with the body are clearly seen. They surround a wide, curved core, identified as the neck, the only head-to-body connection visible in the isolated 30S subunit (Lata et al., 1996; Gabashvili et al., 1999a).

Comparison of our structure with the X-ray map of the *T. thermophilus* 30S subunit (Clemons et al., 1999) allows us to identify a number of structural elements whose appearance is virtually identical in both maps although their relative positions change (see below). Similarities are seen especially well when the cryo-EM map is displayed at a higher threshold for which the volume is estimated to enclose mainly RNA mass. The conformation of the long vertically running helix, identified as helix 44 of 16S RNA in the X-ray maps (Cate et al., 1999; Clemons et al., 1999), appears practically the same, except that it is slightly longer, consistent with the 5 nucleotide difference in secondary structure, and that it shows a slight kink close to the 1430/1470 bulge where bridge B5b (see section on Intersubunit Bridges below) connects. Two structures coming up from the shoulder, looking similar in both X-ray (Cate et al., 1999; Clemons et al., 1999) and cryo-EM maps (marked as * and # in Figure 3c), are clearly seen as differently positioned in all three maps. While only one of these structures (*) participates in the head-to-shoulder contact in the cryo-EM map of the 70S ribosome and the X-ray map of the isolated 30S subunit (Clemons et al., 1999), both appear to interact with the head in the X-ray map of the 70S ribosome (Cate et al., 1999). The truncated appearance of a major head domain in the X-ray map of the subunit (Clemons et al., 1999) could be due to disorder, while the enlarged form of the shoulder structure contacting the head (marked # in Figure 3c; Cate et al., 1999) could be due to difficulties in finding the correct molecular boundary (see Schlünzen et al., 1999).

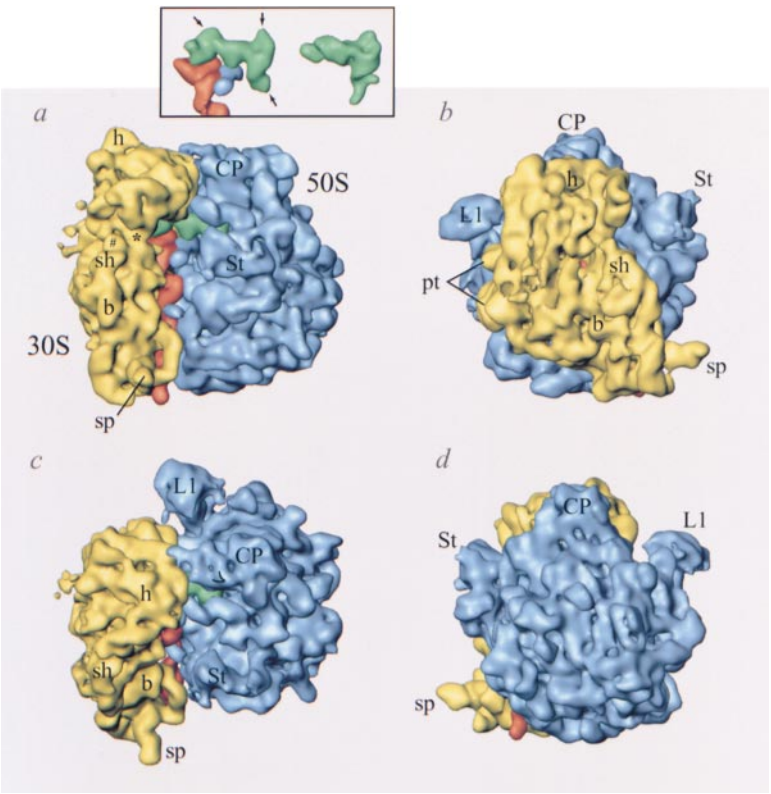

Figure 2. The 11.5 Å Resolution Cryo-EM Map of the *E. coli* 70S Ribosome

The cryo-EM map is shown in (a) subunit–subunit side view, (b) 30S subunit solvent–side view, (c) top view, and (d) the 50S subunit solvent–side view. Domains and features of the 30S subunit (yellow, with helix 44 shown in red) and 50S subunit (blue) are as follows: b, body; h, head; pt, platform; sp, spur; sh, shoulder; St, stalk base; L1, protein L1; and CP, central protuberance. * and # mark sites of the shoulder contacting the head in Cate et al., 1999. V marks the v-shaped structure possibly representing helices of the 5S rRNA. Inset (upper left) displays cryo-EM map of the fMet-tRNA$_f^{Met}$ (green), with arrows pointing to sites interacting with ribosomal components (left), and the expected appearance of fMet-tRNA$_f^{Met}$ (Schmitt et al., 1998) at ~10 Å resolution (right).

50S Subunit

Among easily distinguishable RNA helices is the one bearing the L1 protein (Figure 2, Figure 3, top and center), partially truncated in the X-ray map (Ban et al., 1999). Other well-defined helices can be seen on the solvent side, next to the central protuberance (CP) of the subunit (Figures 2a and 2c). Helical-appearing structural elements of the 50S subunit making contact with helix 44 of the 16S RNA (Figure 3, top and bottom) and others located at the interface (Figure 3, center) are identified as RNA helices in the interpretation of the 5 Å X-ray map (Ban et al., 1999). Variations in the 23S RNA secondary structure among the species are recognizable in some regions of the subunit. It is clearly seen in the case of helix 63 (localized by Spahn et al., 1999), known to be 22 (*H. marismortui*) or 16 (*T. thermophilus*) nucleotides longer in *E. coli*. There are some notable differences in the conformations between elements with close secondary structure, e.g., the helices of the CP (Figure 2): two strands connected in a V-shaped arrangement (marked V in Figure 2c) are aligned perpendicularly to the interface, interacting with the head of the 30S subunit (also see Cate et al., 1999). In the X-ray map of the isolated 50S subunit (Ban et al., 1999) these helices point upwards, toward the top of the CP. The most striking differences are seen in the intersubunit region where the cryo-EM map contains helical strands pointing away from the 50S, toward the 30S, participating in the formation of intersubunit bridges (Figure 3, center: B1a, B2a, B3 in the nomenclature introduced below). In the X-ray structure of the 50S subunit from *H. marismortui* (Ban et al., 1999), the corresponding strands are bent to run close to the intersubunit surface, as though confined by the crystal packing.

Intersubunit Bridges

Several intersubunit bridges were described earlier in low-resolution maps of the *E. coli* ribosome (Frank et al., 1995a; Lata et al., 1996). These bridges are sharply resolved in the present 11.5 Å map, in some cases into several thinner bridges (Figure 3). To characterize them, we use the previously introduced nomenclature B1–B6 (Frank et al., 1995a; Lata et al., 1996), further elaborated by Cate and coworkers (1999).

The earlier-identified bridge B1 between the head of the 30S subunit and the CP of the 50S subunit is now seen to comprise three minor connections, named B1a, B1b, and B1c. B1b and B1c spring from the CP, where the 5S rRNA is located, while B1a is closer to the L7/L12 stalk base and is clearly associated with a 23S RNA helix.

Another bridge previously identified, B2, involving an extended contact between the platform of the 30S subunit and the rim of the interface canyon of the 50S subunit (Frank et al., 1995a; Lata et al., 1996), is now resolved into five separate connections, B2a–B2e. The position of B2a is at the point where helix 44 of the 16S RNA merges with the platform. This upper portion of the helix is directly involved in the formation of the strongest bridging connection between the subunits. Bridges B2b–B2e are associated with other helical structures of the platform. B2d and B2e evidently belong to the same helix positioned at the upper edge of the platform. B2a, B3, B5a, and B5b are formed by four strands of density projecting off the central interface region of the 50S subunit, interacting with four areas of closest approach along h44 of 16S RNA on the interface side of the 30S subunit (Figure 3). B4 was already very well resolved in a lower-resolution map (Frank et al., 1995a).

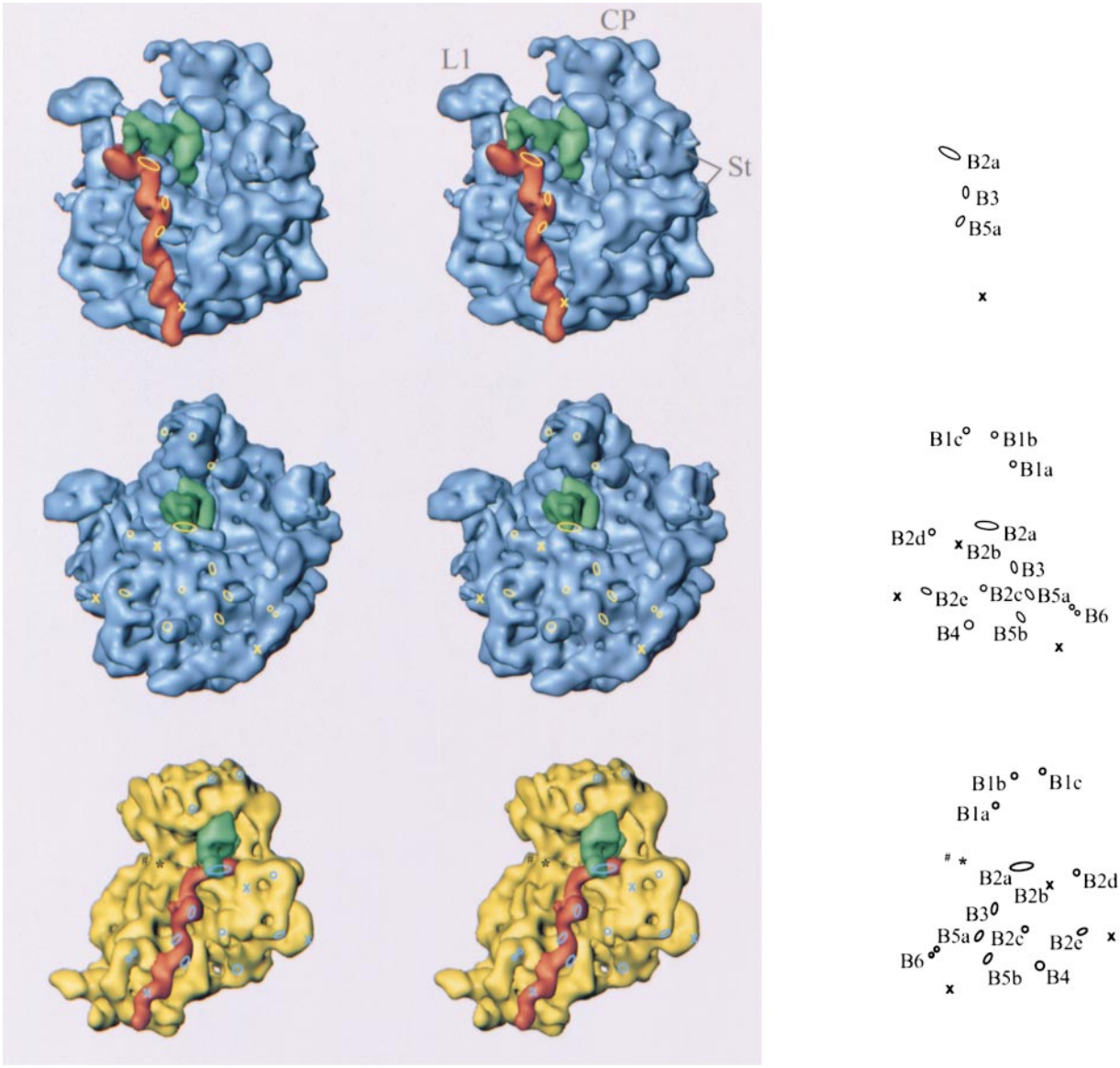

Figure 3. Stereo Views of Large and Small Subunit after Separation of the Ribosome Map

Stereo views of large (top and center panels) and small (bottom panel) subunits, as would be seen from the intersubunit space, obtained by separation of the 70S ribosome map. The portion of the map identified as helix 44 of 16S RNA, which is involved in the association of the subunits, is displayed in red in top and bottom panels. The density attributed to initiator tRNA is shown in green. The arrangement of intersubunit bridges (open circles) is shown on the right of all three panels as mirror-related footprints that can be superimposed on the corresponding subunit views. X marks regions of close contact that do not form a bridge. Other landmarks are the same as introduced in Figure 2.

Finally, a low-density contact in the lower part of the 30S subunit earlier identified as B6 (Frank et al., 1995a) is now seen to involve two different structures. This bridge is absent in the *T. thermophilus* 70S ribosome, though Cate and coworkers (1999) apply this label to another, apparently unrelated structure at a different location.

Placement of Known X-Ray Structures of Ribosomal Components

Each element (protein, RNA helix, or RNP fragment) was docked into the cryo-EM map independently using both Iris Explorer and O (Jones et al., 1991), with initial guidance provided by the placements of Clemons and coworkers (1999) for the 30S subunit, and of Ban and coworkers (1999) and Agrawal and coworkers (2000) for the 50S subunit.

Proteins and rRNA Fragments of the 30S Subunit

All helices of the 16S RNA central domain traced in the X-ray map of the isolated 30S subunit (Clemons et al., 1999) were identified in the cryo-EM map. Helices 19 and 27 (numbering by Müller and Brimacombe, 1997) are continued by a long strand apparently including helices 2 and 28, which form the neck of the subunit. The three-way junction of helices 20, 21, and 22, interacting

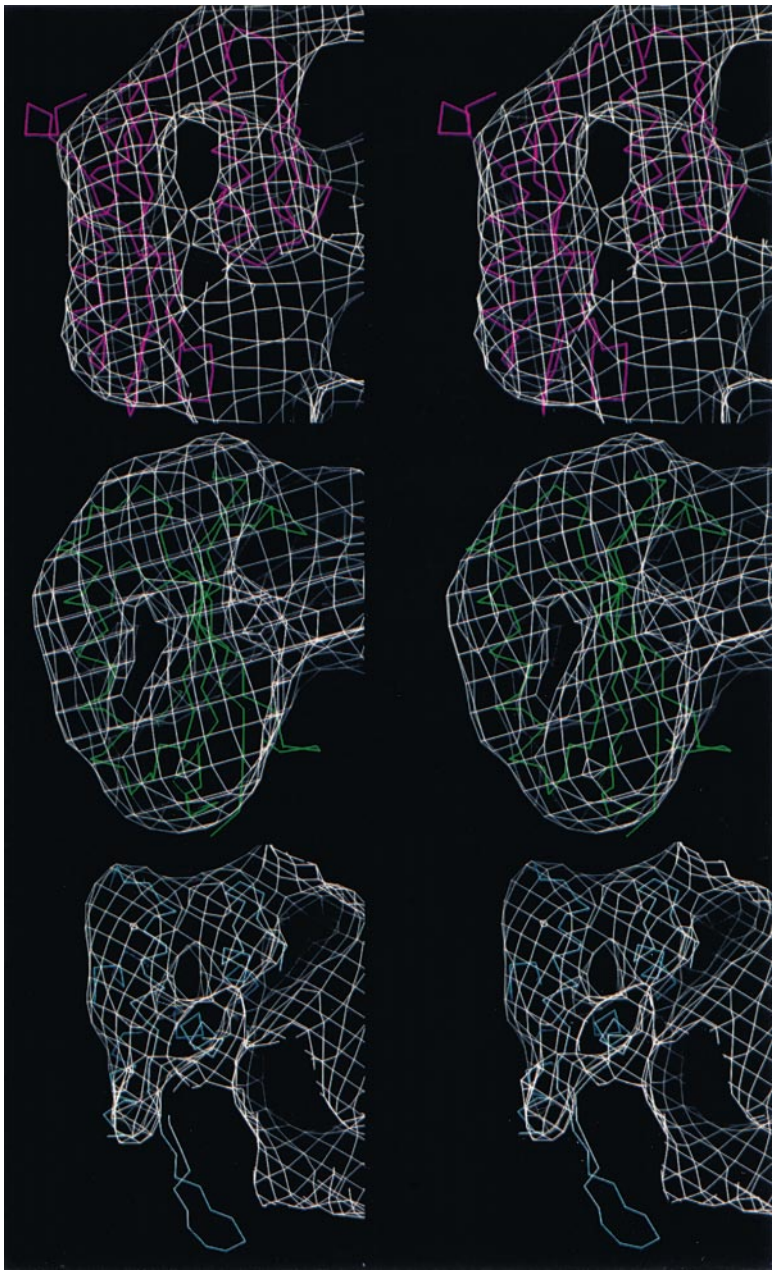

Figure 4. Examples for Fittings of Proteins into the Cryo-EM Density Map

Fittings of protein crystal structures (carbon backbones) into the cryo-EM density (white, wire-mesh), displayed in stereo. Top, S5 (Ramakrishnan and White, 1992); center, S6 (Lindahl et al., 1994); bottom, S7 (Hosaka et al., 1997; Wimberly et al., 1997). These protein structures are displayed on the 30S subunit map in Figure 5 in corresponding colors.

with protein S15, was found to lie in the vicinity of bridge B4. Relative positions of h44, h27, and P site tRNA modeled by Cate and coworkers (1999) showed a very good agreement with the positions of the corresponding elements in the cryo-EM map.

The following proteins were placed: S4, S5, S6, S7, S8, and S15 (Figure 5). In the case of structures identified by Clemons and coworkers (1999) as S17 and S20, the interior boundaries are poorly defined in our map, precluding an accurate fitting. Stereo pairs showing the fittings of three proteins (S5, S6, S7) are shown in Figure 4. Except for the apparently flexible loop region of S7, the overall shape and features of these proteins, all located on the surface of the 30S subunit, are as would be expected at 11.5 Å resolution.

Proteins and rRNA Fragments of the 50S Subunit

Components of the 50S Stalk Base Region. A bilobed region of the large subunit commonly referred to as the stalk base is formed, in major part, by two functionally important components: (1) the thiostrepton-binding L11–23S RNA (58 nt) fragment (upper lobe in Figures 6 and 7) and (2) L6 and the α-sarcin-ricin loop (lower lobe) (see Ban et al., 1999; Agrawal et al., 2000).

Areas of contact between elongation factor G and this region were determined by cryo-EM of several EF-G·ribosome complexes (Agrawal et al., 1998, 1999a). Fitting of the crystal structure of the EF-G domains (Agrawal et al., 1998, 1999c) along with hydroxyl-radical probing (Wilson and Noller, 1998) helped in the placement of ribosomal components interacting with EF-G

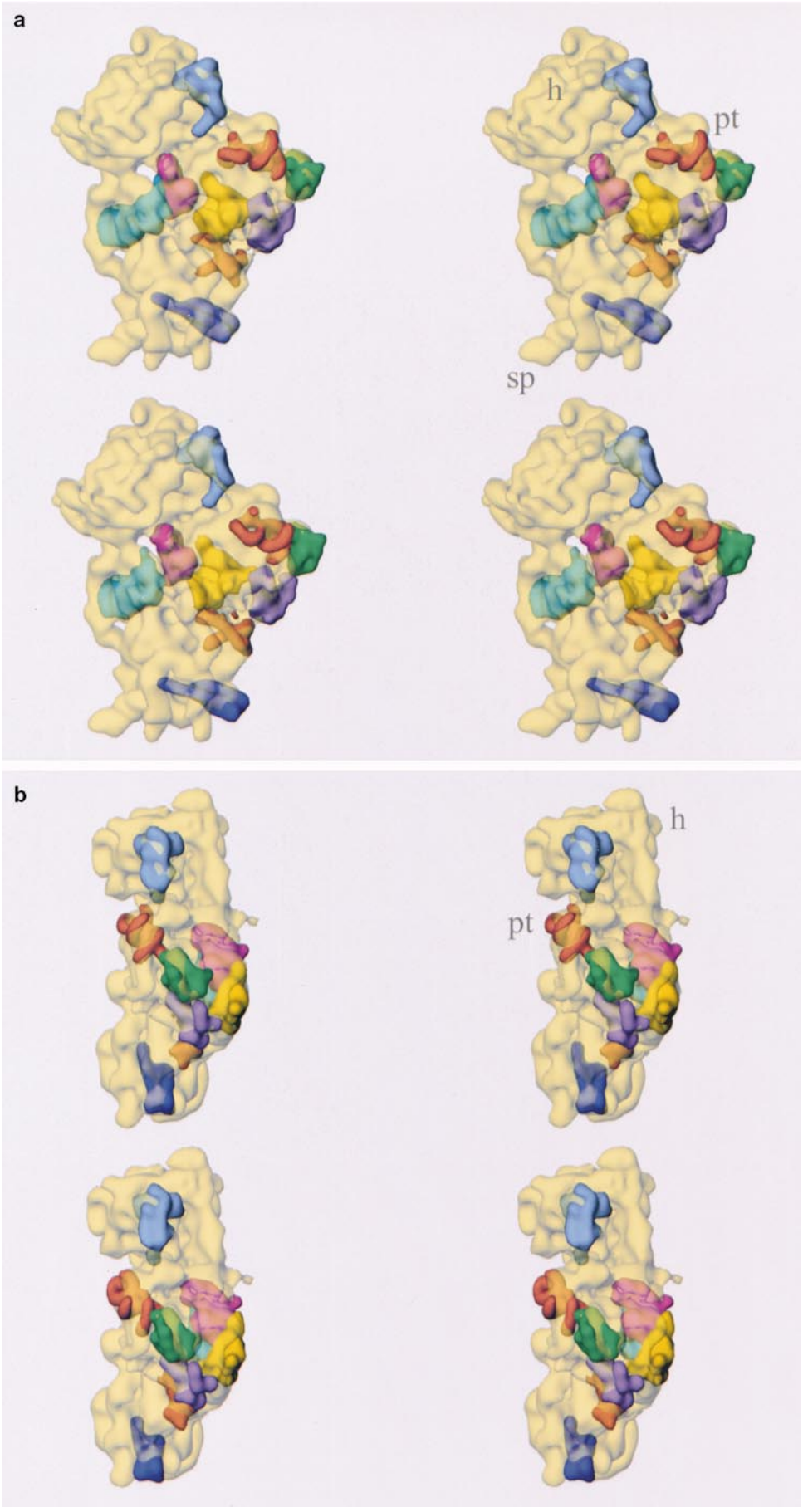
a
h
pt
sp
b
h
pt

(Agrawal et al., 2000). In that work, the X-ray structure of the α-sarcin-ricin loop (Correll et al., 1998) and that of an L11-RNA complex (Wimberly et al., 1999) were fitted into the 15 Å map of the ribosome (Malhotra et al., 1998). Those fittings have been further refined in the new 11.5 Å map (Figure 6a). The 58-nucleotide RNA fragment (shown in blue) along with the L11 protein (green) are completely covered by the cryo-EM densities, including the N-terminal domain of L11, which is not observed in the X-ray map (Ban et al., 1999). The cryo-EM map clearly defines the shape of both domains of L11 (Figure 6a), which was directly localized in this part of the stalk by recent cryo-EM reconstructions of an L11-lacking mutant of the ribosome (R. K. A., J. Linde, K. H. Nierhaus, J. F., unpublished). The position of L11 reveals that the observed arc-like connection (Agrawal et al., 1998, 1999a) involves the G′ domain of EF-G and the N-terminal domain of L11 (see Figure 7).

Among various other EF-G domains, the G domain and domain V also make direct contacts with the base of the stalk. Fitting of the X-ray structure of the EF-G·GDP complex (Czworkowski et al., 1994) into the cryo-EM density corresponding to EF-G (Agrawal et al., 1999a) revealed an unoccupied region near the G domain in the cryo-EM density. This region, which makes contact with the tip of the α-sarcin-ricin loop structure (see below), probably corresponds to disordered 24–amino acid residues in the X-ray structure. Domain V of EF-G makes contact with the groove-shaped region between the 58-nucleotide 23S RNA fragment and the N-terminal domain of L11 protein (Wimberly et al., 1999).

A 23S RNA region of particular interest is the α-sarcin-ricin loop (SRL), because of its crucial roles in the elongation factor–dependent activities of both prokaryotic and eukaryotic ribosomes. Its immediate neighbors are L6 and L14 (Ban et al., 1999). All three elements are located in the stalk base region, with SRL sharply delineated on account of its higher-density S turn profile (yellow in Figure 6a). In the fitting of SRL we used X-ray structures both from rat (Correll et al., 1998) and *E. coli* (Correll et al., 1999). The latter gives a better fit due to the absence of one base pair in the flexible region and a changed arrangement between stem and loop region. Thus, the small structural differences observed in the X-ray maps of SRL fragments (Correll et al., 1999) can also be identified in the context of the ribosome matrix.

In locating L6 and L14, we were guided by the placement of Ban and coworkers (1999). Shape and features of the L6 protein, which was slightly modified by Ban and coworkers (1999), are recognizable in the surrounding stalk base densities (green in Figure 6a). L6 (aa 103) is found in close proximity to a minor groove of SRL, near base 2667, with the long axis of L6 running approximately perpendicular to SRL. On the other side, SRL is flanked by L14 but forms no direct contact with it. The placement of this protein by Ban and coworkers (1999) indicates its involvement in the formation of bridges B5a and B6.

L1 Protein. Previously, the X-ray structure of this protein from *T. thermophilus* (Nikonov et al., 1996) was fitted into the 15 Å map of the 70S ribosome (Malhotra et al., 1998), based on shape constraints. At the current level of resolution, fitting of X-ray coordinates can be guided by subdomain details of the protein structure. Moreover, the relative orientation of the two L1 domains appears to be different from the orientation they possess in the X-ray structure, which depicts the protein without RNA interaction. To obtain the best fit (Figure 7), we therefore had to rotate domain II by about 15 degrees, using the interdomain-connecting regions as hinges. It was previously shown that L1 protein has a different conformation in the ribosomal crystal structure when compared with the cryo-EM map (Ban et al., 1998; Penczek et al., 1999).

Comparison of Placements of Various rRNA Helices and Proteins in Cryo-EM versus 5 Å X-Ray Maps

Obtaining a Common Frame of Reference

At the time of preparation of this article, none of the electron densities of the recently published X-ray structures were available. Thus, in order to compare the cryo-EM map with the X-ray maps of individual subunits, the atomic coordinates of proteins and RNA elements fitted to the relevant density maps were used (available from the Protein Data Bank).

In the case of 30S, the docking (see previous section on Placement of Known Structures) was done for proteins S4, S5, S6, S7, S8, S15, S17, and S20, as well as helices 20, 21, 22, 23, 24, 27, and 44. The full set of atomic coordinates obtained was treated as a rigid body and overlapped with the model of Clemons and coworkers (1999) using a least-squares transformation, including changes of scale, translation, and rotation. After outliers (S4, S6, h23) and fittings of high uncertainty (S17, S20) were removed, the least-squares fitting was repeated. To evaluate the extent of any discrepancies, a root-mean-square deviation (rmsd) was calculated between atomic coordinates of the model derived from the X-ray map and the transformed coordinates of the fittings performed on the cryo-EM map. This overall rmsd was 4.5 and 5.4 Å with two independent sets of fittings. In addition, an rmsd value was calculated for each of the proteins and helices, which was decomposed into two parts, attributed to translation and rotation, respectively.

In the case of the 50S subunit, the analysis described above was applied to the following four elements: the α-sarcin-ricin loop (SRL), protein L6, the RNA portion of the thiostrepton-binding L11/23S RNA fragment (Wimberly et al., 1999), and the C-terminal domain of L11

Figure 5. Positions of Fitted Proteins and 16S RNA Helix 23 in Cryo-EM and X-Ray Map of the 30S Subunit

Semitransparent stereo representations of the 30S subunit cryo-EM density map, showing the positions of some of the proteins and helix 23, as fitted into the cryo-EM map (top panels) and into the X-ray map (Clemons et al., 1999) (bottom panels). The relative positions between coordinates derived from fittings into cryo-EM and X-ray maps were obtained by an overall least-squares fit (see text). (a) view of the subunit from the interface side, (b) from the side of the platform (i.e., from the right in [a]). Color coding: h23, red; S4, blue-green; S5, magenta; S6, green; S7, light blue; S8, yellow; S15, violet; S17, orange; S20, dark blue. Landmarks: h, head; pt, platform; sp, spur. (Models of S17 and S20 were derived from C-α coordinates, all others from all-atoms coordinates.)

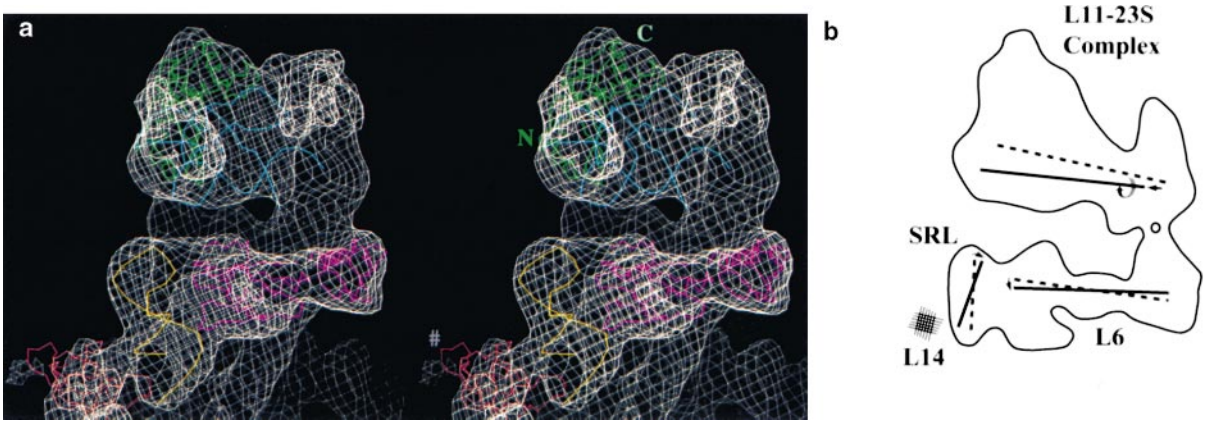

Figure 6. Architecture of the GTPase-Associated Center, and Its Rearrangement

(a) Closeup on the stalk base region of the 50S subunit, along with fittings of PDB coordinates of three components, displayed in stereo. These fittings were obtained using all-atom coordinates; however, only backbones are shown for clarity. Yellow, α-sarcin-ricin loop (SRL; Correll et al., 1999); magenta, protein L6; green and blue, L11 (green)/23S RNA fragment (blue) (Wimberly et al., 1999). Orange, L14, whose placement was adopted from Ban and coworkers (1999). # points to the proximity of mass corresponding to bridge B5a and a portion of L14. N and C indicate N- and C-terminal domains of protein L11, respectively.

(b) Schematic diagram depicting the changes in the positions of SRL, L6 and L11-23S complex from X-ray fittings (*H. marismortui*, Ban et al., 1999; dashed line) to those obtained for the 11.5 Å cryo-EM map (*E. coli*). The outline shown is the boundary of the two lobes of the stalk base density map as it appears in the plane in which the three fitted components lie. The lines indicate, respectively, the position of the helix axis for SRL, the approximate position of the long axis for L6, and a line joining the stem containing the 5′ and 3′ ends of the RNA (58 nt) fragment (on the right) with the center of L11 (on the left). Circle represents the peripheral hinge point between the two lobes of the stalk base.

(Conn et al., 1999), using the placements supplied by Ban and coworkers (1999) for comparison. In this case, the overall rmsd was 3.4 Å.

30S Subunit

Fittings of various proteins and RNA fragments into the 30S portion of the cryo-EM map are presented in Figure 5. For comparison, the fittings of the same components into the X-ray map (Clemons et al., 1999) are also shown in the framework of our map (bottom panels in Figures 5a and 5b). It can be seen in the side view (Figure 5b) that the general direction of changes in position, going from the X-ray fittings to our fittings, is inward. S4, situated on the shoulder, a portion of which forms the border of the mRNA channel, moves in the direction of the channel toward the 50S subunit. S6, which is located on the lower lobe of the bilobed platform, moves by ~6 Å away from the 50S subunit, while helix 23, which forms the rim of the upper lobe, moves by ~10 Å in the same direction. The different sizes of these movements define a twist of the underlying platform structure, which curls toward the head of the 30S subunit. Helix 23 is instrumental in the association of the subunits and evidently participates in the formation of bridges B2d and B2e. The same change in platform morphology was observed when we compared the density maps of the isolated and the 50S-bound 30S (Lata et al., 1996; Agrawal et al., 1999b).

The shift of S7 (head portion) by >5 Å toward the 50S subunit is probably associated with a slight movement of the 30S head in that direction, again in agreement with a conformational change upon subunit association (Agrawal et al., 1999b). Finally, S20 (modeled by Clemons et al., 1999), which could not be fitted because of the lack of internal features in this region of our map, can nevertheless be recognized by the shape of its boundary. Its placement in the X-ray map is clearly in conflict with our map since it protrudes from it by almost 10 Å. Thus S20, located close to the lower end of h44, indicates a major rearrangement in that part of the two maps. The main thrust of the rearrangement is an inward movement of S20 from its more protruding position in the X-ray map, roughly following a diagonal direction.

50S Subunit: Region of GTPase-Associated Center

One of the most interesting changes between the cryo-EM and X-ray structure of the 50S subunit, from a functional point of view, takes place in the constellation formed by the α-sarcin-ricin loop (SRL), proteins L6, and L14. The most substantial change when going from the X-ray to the cryo-EM map is a rotation of the helix axis of SRL by 17° in the plane of Figure 6a around a point located on the upper half of the helix axis. In addition, we observe a minor rotation (~6°) of L6 in that same plane (Figure 6b). The movement of SRL brings its 3′ and 5′ ends closer to protein L14. When comparing the relative positions of the L11/23S rRNA fragment with respect to the tip of SRL in the two maps, we find a shift, by 8 Å, in the direction of L11 (horizontal in Figure 6) accompanied by a rotation of 10.5°, effectively narrowing the distance between the two structures by ~10 Å as we go from the X-ray to the cryo-EM map. Since these two components of the 50S subunit are sitting in two distinct lobes of the stalk base, their relative movement is associated with a relative twisting movement of the lobes around a peripheral flex point (marked with a circle in Figure 6b).

Discussion

Assignments of Interface Elements Forming the Bridges

Available biochemical information and existing rRNA models, as well as recent placements in crystallographic maps (Ban et al., 1999; Clemons et al., 1999) and analysis of bridging connections in *T. thermophilus* (Cate et al.,

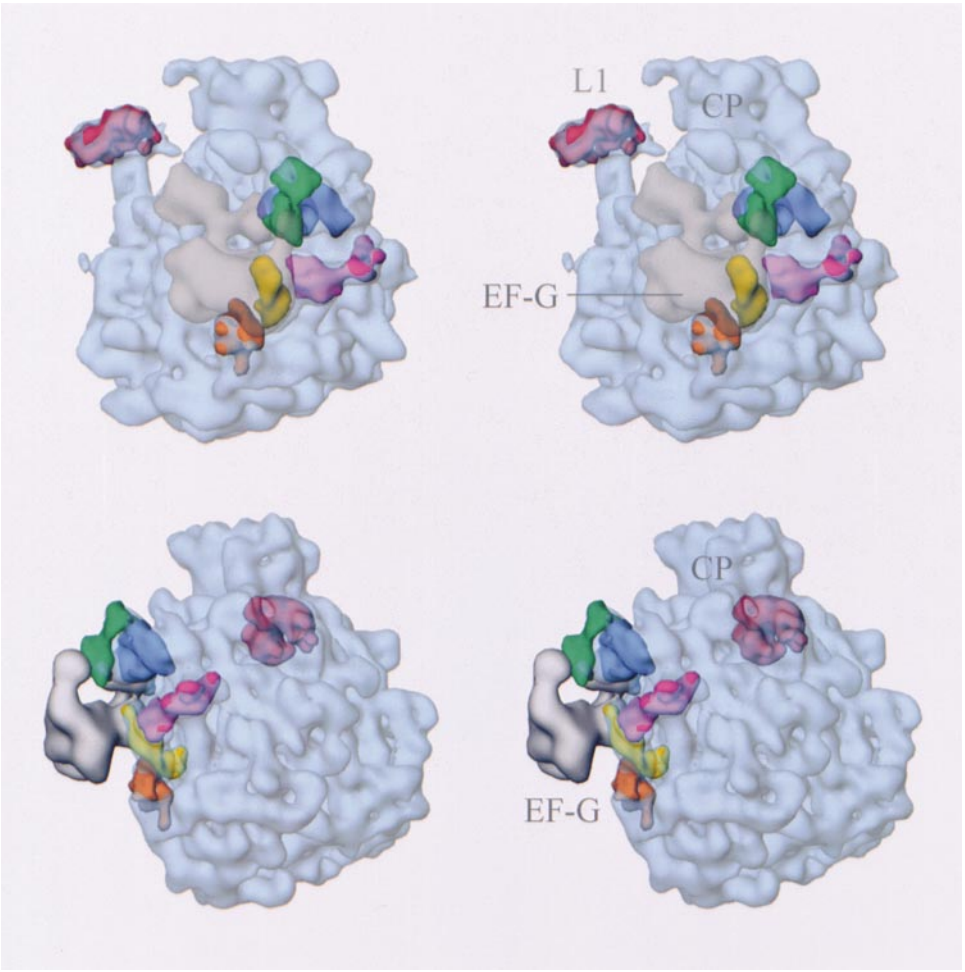

Figure 7. Positions of Fitted Proteins, RNA Fragments, and Elongation Factor G in the 50S Subunit

Semitransparent stereo representation of the 50S subunit cryo-EM density map (light blue), showing the fitted positions of proteins and RNA fragments at the GTPase-associated center, as well as L1. Color coding: red, L1; magenta, L6; orange, L14; green, L11; blue, 58 nt 23S RNA fragment (Wimberly et al., 1999); yellow, α-sarcin-ricin loop; semi-transparent gray, density corresponding to EF-G in the ribosome·$(tRNA)_2$·EF-G·GDP·fusidic acid complex (Agrawal et al., 1999a). EF-G is seen to contact the tip of the α-sarcin-ricin loop with its GTP-binding domain, and the N-terminal domain of L11 with the tip of its G domain (Agrawal et al., 2000). Landmark: CP, central protuberance.

1999) help to identify structural elements forming the intersubunit bridges in *E. coli* ribosome (Figure 3).

Several bridging connections of the ribosome have been unambiguously identified in the recent paper of Cate and coworkers (1999). Bridge B4 has been shown (Culver et al., 1999) to be formed by protein S15 and helix 34 of the 23S RNA. The participation of helices 44 of the 16S RNA and 69 of 23S RNA in the construction of B2a, and of helices 23, 24, and 27 of the 16S RNA in forming B2b (h24), B2d (h23.2), B2e (h23.1), and B2c (h27) is also known (see Cate et al., 1999). The corresponding contacting structures from the 23S RNA are possibly h68 and h71. We believe that bridges B2b and B2d are formed by a single helix, h68, as, on the one hand, it is the closest neighbor of h69 (B2a) and, on the other hand, it has been cross-linked both with protein L1, localized in the vicinity of this bridge, and with tRNAs located close to this part of the interface canyon (Osswald et al., 1990, 1995). Some of the B2 bridges with the 30S subunit platform could involve portions of the large proteins L2 (B2e) and L3 (B2c) of the 50S subunit and S11 (B2d) of the small subunit. L2 and S11 have been cross-linked to each other (Lambert and Traut, 1981), as well as to the bridge-forming (h23 of 16S RNA) or neighboring (h64 of 23S RNA) helices (Osswald et al., 1990). These three proteins are known to play pivotal functional roles in protein synthesis that require a high degree of coordination: L2 is associated with the peptidyl-transferase activity (Wittmann-Liebold, et al., 1995), S11 has been implicated in tRNA selection (Fanning et al., 1978), and L3 in controlling maintenance of the mRNA reading frame in particular cases (Peltz et al., 1999).

Participation of L2 in bridge B2e is supported by the placement of L2 by Ban and coworkers (1999). This bridge is absent in the 70S map of *T. thermophilus* (Cate et al., 1999), although in *E. coli* we do observe a very strong connection of this 50S subunit region with the 16S RNA helix h23. This may be one of the species-related differences between mesophilic and thermophilic 70S ribosomes.

According to protection data (Merryman et al., 1999),

helix 38 of 23S RNA is the most likely candidate for bridge B1a. This structure was identified earlier as long bridge (Malhotra et al., 1998), or A site finger (Stark et al., 1997a) in a truncated form.

Bridge B6 is located near the variable loop of h44 of the 16S RNA. The participating structural elements of the 50S subunit are seen in the cryo-EM map as belonging to two different but neighboring structures. The lower strand is in the immediate neighborhood of helix 63 of the 23S RNA (identified by genetic tagging and cryo-EM; Spahn et al., 1999). Thus, it may involve neighboring nucleotides in the RNA secondary structure (shown to cross-link with proteins L19 and L14). The upper structure participating in the formation of this bridge from the 50S side may represent protein L14 (Ban et al., 1999). Bridge B6 is absent and replaced by another bridge in *T. thermophilus* located on h44, apparently providing a restraint for the movement of this helix at the subunit–subunit interface.

Dynamic Nature of Connections between the Subunits

Comparison of the cryo-EM map with the recent X-ray maps of the extremophile ribosomes (Ban et al., 1999; Cate et al., 1999; Clemons et al., 1999), along with recent results showing rearrangement of bridges in the *E. coli* ribosome (Gabashvili et al., 1999b), indicates movements in these bridging elements in the ribosomal interface. The most interesting region in this respect is the penultimate loop, i.e., h44 of the 16S RNAs 3′ minor domain, connected to the 50S subunit in four regions (bridges B2a, B3, and B5a,b). The appearance of these long connections suggests their role in the dynamics of the ribosome, as small changes in the conformation of the contacting 23S RNA helices would result in relatively big displacements of h44 and components of the body of the 30S subunit connected with it. It is highly likely that these structures play a crucial role in the association and cooperative functioning of the ribosomal subunits. The upper portion of h44 participates in the mRNA decoding and controls fidelity of the codon–anticodon interactions along with the mRNA translocation. Of particular importance in this respect is h27, located between B3 and B2c (Clemons et al., 1999; Cate et al., 1999), which switches conformation, thereby modulating translational accuracy (Lodmell and Dahlberg, 1997). Indeed, a recent cryo-EM study of ribosomes from mutants with h27 locked in alternative conformations indicates large rearrangements affecting the position of h44 as well as more distant parts of the ribosome (Gabashvili et al., 1999b). B1b and B1c were seen to change their architecture in this transition from one proofreading state to the other. Comparison with the X-ray structure of the unbound 30S subunit (Clemons et al., 1999) indicates a shift of helix 44 upon subunit–subunit association. Presumably, this helix serves as a binding sensor, promoting the 30S–50S subunit association and initiating structural rearrangements of the decoding region.

The absence of intersubunit cross-links and regions protected by subunit–subunit association in the head of the 30S subunit is in accordance with the observed relative mobility of this domain (Gabashvili et al., 1999b; Agrawal et al., 2000).

Interpretation of Conformational Changes

The changes in positions of proteins fitted into the 30S part of the 70S cryo-EM map from *E. coli* compared to those reported for the isolated 30S subunit from *T. thermophilus* (Clemons et al., 1999) can be explained on the basis of an architectural rearrangement of the subunit apparently required for its association with the 50S subunit. These changes involve a curling-in of the platform toward the head of the 30S subunit (thereby creating a channel for the upstream region of mRNA; see Frank et al., 2000b) and a shift of the head toward the 50S subunit (Lata et al., 1996; Agrawal et al., 1999b). It is likely that the nature of this rearrangement is the same for *T. thermophilus*, as far as it can be judged from a visual comparison with published X-ray maps (Cate et al., 1999; Clemons et al., 1999).

To assess the significance of the observed changes in the region of the GTPase-associated center, it is necessary to recall all the aspects in which the cryo-EM map differs from the X-ray map: (1) species (*H. marismortui* versus *E. coli*): it is unlikely that difference of this size will occur in one of the most conserved, functionally important regions of the ribosome; (2) crystal packing (crystal versus solution structure): the size and nature of the SRL movement argue against such an explanation; however, crystal packing forces cannot be ruled out as an explanation for the rearrangement of the peripherally located lobes of the stalk base that gives rise to the change in the distance between SRL and L11/23S rRNA; (3) free versus 30S-bound 50S subunit; (4) tRNA-bound versus unbound ribosome. The two last factors are likely to be the most important in explaining the observed conformational rearrangement. Since the cryo-EM structure shows the ribosome in a defined state (initiation-like), it is quite possible that the X-ray map of the isolated large subunit (Ban et al., 1999) could represent another conformational state along the elongation cycle.

The effect of the SRL rotation on L6 is that it changes the geometry of the contact zone between the two structures. Since L6 and the L11/23S rRNA structure are interconnected and strategically located in the region of the stalk base, their movements are likely to produce changes in the orientation of the L7/L12 stalk, which may in turn cause relatively large changes in the position of the stalk tip. On the side opposite L6, the decrease in distance between SRL and protein L14 brought about by the rotation of SRL is noteworthy because of the participation of L14 in forming two bridges spanning the two subunits, B5a and B6. Thus, the formation of the contact between SRL and L14 could be part of the dynamic signaling that is thought to coordinate the actions at the decoding region of the 30S subunit with that of the centers of the 50S subunits GTPase and peptidyltransferase activities.

Experimental Procedures

Microscopy and Image Acquisition

Initiation-like fMet-tRNA$_f^{Met}$-ribosome complexes were prepared for cryo-microscopy as described by Malhotra and coworkers (1998). Micrographs were recorded using low-dose protocols (10e$^-$/Å^2) on a Philips CM200 C1 field emission gun (FEG) electron microscope at 200 kV and a nominal magnification of 51,200×. They were checked for drift, astigmatism, and presence of Thon rings by optical

diffraction, and scanned on a Perkin Elmer PSD 1010A microdensitometer using a step size of 15 μm, corresponding to 2.93 Å on the object scale.

Image Processing

Ribosomes were selected by a quasi-automated selection procedure (Lata et al., 1995) and by direct comparison of the particle candidates with the reference set of 83 projections (Penczek et al., 1994) of the existing map of the fMet-tRNA$_f^{Met}$ complex (Malhotra et al., 1998). A subset of particles was chosen based on the size of the cross-correlation coefficient and was further reduced following visual inspection to a final set of 54,479.

The CTF parameters were initially calculated based on the power spectrum estimated from each micrograph using the method of averaged overlapping periodograms (Zhu et al., 1997). All particles were sorted according to defoci derived from CTF analysis and placed into 23 groups. The defoci ranged from 2.17 to 4.34 μm and the number of particles per group ranged from 974 to 3831. The same analysis was repeated for the previously published set of fMet-tRNA$_f^{Met}$-ribosome particles (Malhotra et al., 1998), from which 19,044 best-quality particles were selected. They were placed in additional eight defocus groups with defoci ranging from 0.73 to 2.32 μm and the number of particles per defocus group ranging from 860 to 3300. Since this data set was collected on a different microscope (Philips EM 420 at 52,200× magnification), the pixel size was adjusted and additional normalization of the data set was performed.

The total set of 73,523 particles was subjected to 3D projection alignment, as described in Frank et al., 2000a. The refinement was repeated eight times with the angular step gradually decreasing from the initial 2.0° to 0.2° for the final step. During the refinement an additional verification and adjustment of CTF parameters were performed. After CTF correction (Frank and Penczek, 1995), the estimation of resolution was done by randomly splitting the data set into two groups, calculating separate volumes, and comparing them in Fourier space using the Fourier shell correlation (van Heel, 1986).

All steps of image processing were performed using the SPIDER image processing system (Frank et al., 1996). Computations for refinement and 3D reconstruction were done on the Origin 2000 (Silicon Graphics, Mountain View, CA).

Correction of the Fourier Amplitudes

Synchrotron radiation X-ray scattering data were collected using standard procedures on the X33 camera of the EMBL on the storage ring DORIS III of DESY and multiwire proportional chambers with delay line readout (Koch and Bordas, 1983; Boulin et al., 1988). The samples were measured at 70S ribosome concentrations of 5 and 20 mg/ml in the same buffer as used for EM studies. Scattering data were recorded at sample-detector distances of 3.9 and 1.4 m covering the momentum transfer ranges $0.01 < s < 1.7$ nm^{-1} and $0.03 < s < 5.4$ nm^{-1}, respectively ($s = 4\pi \sin\theta/\lambda$, where $\lambda = 0.15$ nm is the X-ray wavelength and 2θ the scattering angle). The data were normalized and processed using the program SAPOKO (D. I. S. and M. Koch, unpublished), and the processed curves at the two sample-detector distances were merged to yield a composite scattering curve. The latter was further processed using the indirect Fourier transform program GNOM (Svergun et al., 1988) to compute the distance distribution function in the range $0 < r < 27$ nm. A sine Fourier transformation of this function yielded the final smoothed, extrapolated scattering intensity up to 1/7.85 Å^{-1}. Comparison between the final X-ray scattering intensity distribution and the power spectrum of the cryo-EM map (Figure 1) shows a falloff toward higher spatial frequencies. Fourier amplitudes of the density map were multiplied by the square root of the ratio of these curves before application of a low-pass filter to limit the resolution to 11.5 Å.

Visualization and Interpretation of 3D Maps

Extraction of 3D elements from the final volumes was done using SPIDER with the help of Tinkerbell (Li et al., 1997) and IRIS Explorer (Numerical Algorithms Group, Inc., Downers Grove, IL). Visualization of the density map and docking of X-ray crystal structures was done using IRIS Explorer and O (Jones et al., 1991). For docking in Explorer, the atomic coordinate files were converted into electron density maps by computing averaged densities within volume elements scale-matched to those of the EM map (2.93 Å). Surface representations of these computed density maps were then used. Docking in O was done using a surface representation of the EM map and direct visualization of atomic models imported from the PDB.

Acknowledgments

We thank Knud Nierhaus for providing MF-RNA and fMet-tRNA$_f^{Met}$ and David Stokes from New York University for making a Philips CM200 FEG electron microscope available for our studies. We are grateful to Venki Ramakrishnan for providing all-atom coordinates of the L11-RNA fragment complex. We also thank Arun Malhotra for helpful suggestions in the initial phase of the work, Ardean Leith for writing software for examination of contact surfaces, Gregor Blaha for preparing specimens for solution scattering, and Amy Heagle for preparing the illustrations. Some of the computing support was provided by NCSA, University of Illinois at Urbana-Champaign. This work was supported by grants NIH R37 GM29169, R01 GM55440, and NSF BIR 9219043 (to J. F.).

Received December 13, 1999; revised February 10, 2000.

References

Agrawal, R.K., Penczek, P., Grassucci, R.A., Li, Y., Leith, A., Nierhaus, K.H., and Frank, J. (1996). Direct visualization of A-, P-, and E-site transfer RNAs in the *Escherichia coli* ribosome. Science *271*, 1000–1002.

Agrawal, R.K., Penczek, P., Grassucci, R.A., and Frank, J. (1998). Visualization of elongation factor G on the *Escherichia coli* 70S ribosome: the mechanism of translocation. Proc. Natl. Acad. Sci. USA *95*, 6134–6138.

Agrawal, R.K., Heagle, A.B., Penczek, P., Grassucci, R.A., and Frank, J. (1999a). EF-G-dependent GTP hydrolysis induces translocation accompanied by large conformational changes in the 70S ribosome. Nat. Struct. Biol. *6*, 643–647.

Agrawal, R.K., Lata, K.R., and Frank, J. (1999b). Conformational variability in *E. coli* 70S ribosome as revealed by 3D cryo-electron microscopy. Intl. J. Biochem. Cell Biol. *31*, 243–254.

Agrawal, R.K., Penczek, P., Grassucci, R.A., Burkhardt, N., Nierhaus, K.H., and Frank, J. (1999c). Effect of buffer conditions on the position of tRNAs on the 70S ribosome as visualized by cryo-electron microscopy. J. Biol. Chem. *274*, 8723–8729.

Agrawal, R.K., Heagle, A.B., and Frank, J. (2000). Studies of elongation factor G-dependent tRNA translocation by three-dimensional cryo-electron microscopy. In The Ribosome: Structure, Function, Antibiotics, and Cellular Interactions, R.A. Garrett, S.R. Douthwaite, A. Liljas, A.T. Matheson, P.B. Moore, and H.F. Noller, eds. (Washington, D.C.: ASM Press), pp. 53–62.

Ban, N., Freeborn, B., Nissen, P., Penczek, P., Grassucci, R.A., Sweet, R., Frank, J., Moore, P.B., and Steitz, T.A. (1998). A 9 Å resolution X-ray crystallographic map of the large ribosomal subunit. Cell *93*, 1105–1115.

Ban, N., Nissen, P., Hansen, J.C., Capel, M., Moore, P.B., and Steitz, T.A. (1999). Placement of protein and RNA structures into a 5Å-resolution map of the 50S ribosomal subunit. Nature *400*, 841–847.

Basavappa, R., and Sigler, P.B. (1991). The 3 Å crystal structure of yeast initiator tRNA: functional implications in initiator/elongator discrimination. EMBO J. *10*, 3105–3111.

Böttcher, B., Schwarz, L., and Graber, P. (1998). Direct indication for the existence of a double stalk in CF_0F_1. J. Mol. Biol. *281*, 757–762.

Boulin, C.J., Kempf, R., Gabriel, A., and Koch, M.H.J. (1988). Data acquisition systems for linear and area X-ray detectors using delay line readout. Nucl. Instrum. Methods *A269*, 312–320.

Cate, J.H., Yusupov, M.M., Yusupova, G.Z., Earnest, T.N., and Noller, H.F. (1999). X-ray crystal structures of 70S ribosome functional complexes. Science *285*, 2095–2104.

Clemons, W.M., Jr., Davies, C., White, S.W., and Ramakrishnan,

V. (1998). Conformational variability of the N-terminal helix in the structure of ribosomal protein S15. Structure *6*, 429–438.

Clemons, W.M., Jr., May, J.L.C., Wimberly, B.T., McCutcheon, J.P., Capel, M., and Ramakrishnan, V. (1999). Structure of a bacterial 30S ribosomal subunit at 5.5 Å resolution. Nature *400*, 833–840.

Conn, G.L., Draper, D.E., Lattman, E.E., Gittis, A.G. (1999). Crystal structure of a conserved ribosomal protein-RNA complex. Science *284*, 1171.

Correll, C.C., Munishkin, A., Chan, Y.L., Ren, Z., Wool, I.G., and Steitz, T.A. (1998). Crystal structure of the ribosomal RNA domain essential for binding elongation factors. Proc. Natl. Acad. Sci. USA *95*, 13436–13441.

Correll, C.C., Wool, I.G., and Munishkin, A. (1999). The two faces of the *Escherichia coli* 23S rRNA sarcin/ricin domain: the structure at 1.11 Å resolution. J. Mol. Biol. *292*, 275–287.

Culver, G.M., Cate, J.H., Yusupova, G.Z., Yusupov, M.M., and Noller, H.F. (1999). Identification of an RNA-protein bridge spanning the ribosomal subunit interface. Science *285*, 2133–2135.

Czworkowski, J., Wang, J., Steitz, T.A., and Moore, P.B. (1994). The crystal structure of elongation factor G complexed with GDP, at 2.7 Å resolution. EMBO J. *13*, 3661–3668.

Fanning, T.G., Cantrell, M., Shih, C.Y., and Craven, G.R. (1978). Evidence that proteins S1, S11 and S21 directly participate in the binding of transfer RNA to the 30S ribosome. Nucleic Acids Res. *5*, 933–950.

Frank, J., and Penczek, P. (1995). On the correction of the contrast transfer function in biological electron microscopy. Optik *98*, 125–129.

Frank, J., Verschoor, A., Li, Y., Zhu, J., Lata, R.K., Radermacher, R., Penczek, P., Grassucci, R., Agrawal, R.K., and Srivastava, S. (1995a). A model of the translational apparatus based on a three-dimensional reconstruction of the *Escherichia coli* ribosome. Biochem. Cell Biol. *73*, 757–765.

Frank, J., Zhu, J., Penczek, P., Li, Y., Srivastava, S., Verschoor, A., Radermacher, M., Grassucci, R., Lata, R.K., and Agrawal, R.K. (1995b). A model of protein synthesis based on cryo-electron microscopy of the *E. coli* ribosome. Nature *376*, 441–444.

Frank, J., Radermacher, M., Penczek, P., Zhu, J., Li, Y., Ladjadj, M., and Leith, A. (1996). SPIDER and WEB: processing and visualization of images in 3D electron microscopy and related fields. J. Struct. Biol. *116*, 190–199.

Frank, J., Penczek, P., Agrawal, R.K., Grassucci, R.A., and Heagle, A.B. (2000a). Three-dimensional cryo-electron microscopy of ribosomes. Methods Enzymol. *317*, 276–291.

Frank, J., Penczek, P., Grassucci, R.A., Heagle, A.B., Spahn, C.M.T., and Agrawal, R.K. (2000b). Cryo-electron microscopy of the translational apparatus: experimental evidence for the paths of mRNA, tRNA, and the polypeptide chain. In The Ribosome: Structure, Function, Antibiotics, and Cellular Interactions, R.A. Garrett, S.R. Douthwaite, A. Liljas, A.T. Matheson, P.B. Moore, and H.F. Noller, eds. (Washington D.C.: ASM Press), pp. 45–51.

Gabashvili, I.S., Agrawal, R.K., Grassucci, R.A., and Frank, J. (1999a). Structure and structural variations of the *E. coli* 30S ribosomal subunit as revealed by three-dimensional cryo-electron microscopy. J. Mol. Biol. *5*, 1285–1291.

Gabashvili, I.S., Agrawal, R.K., Grassucci, R.A., Squires, C.L., Dahlberg, A.E., and Frank, J. (1999b). Major rearrangements in the 70S ribosomal 3D structure caused by a conformational switch in 16S ribosomal RNA. EMBO J. *18*, 6501–6507.

Glaeser, R.M., and Downing, K.H. (1992). Assessment of resolution in biological electron crystallography. Ultramicroscopy *47*, 256–265.

Harms, J., Tocilj, A., Levin, I., Agmon, I., Stark, H., Kölln, I., van Heel, M., Cuff, M., Schlünzen, F., Bashan, A., Franceschi, F., and Yonath, A. (1999). Elucidating the medium-resolution structure of ribosomal particles: an interplay between electron cryo-microscopy and X-ray crystallography. Structure *7*, 931–941.

Hosaka, H., Nakagawa, A., Tanaka, I., Harada, N., Sano, K., Kimura, M., Yao, M., and Wakatsuki, S. (1997). Ribosomal protein S7: a new RNA-binding motif with structural similarities to a DNA architectural factor. Structure *5*, 1199–1208.

Jones, T.A., Zhou, J.Y., Cowan, S.W., and Kjeldgaard, M. (1991). Improved methods for building protein models in electron density maps and the location of errors in these models. Acta Crystallogr. A *A47*, 110–119.

Koch, M.H.J., and Bordas, J. (1983). X-ray diffraction and scattering on disordered systems using synchroton radiation. Nucl. Instrum. Methods *208*, 461–469.

Lambert, J.M., and Traut, R.R. (1981). The subunit interface of the *Escherichia coli* ribosome. Identification of proteins at the interface between the 30 S and 50 S subunits by crosslinking with 2-iminothiolane. J. Mol. Biol. *149*, 451–476.

Lata, K.R., Penczek, P., and Frank, J. (1995). Automatic particle picking from electron micrographs. Ultramicroscopy *58*, 381–391.

Lata, K.R., Agrawal, R.K., Penczek, P., Grassucci, R., Zhu, J., and Frank, J. (1996). Three-dimensional reconstruction of the *Escherichia coli* 30 S ribosomal subunit in ice. J. Mol. Biol. *262*, 43–52.

Li, Y., Leith, A., and Frank, J. (1997). Tinkerbell—a tool for interactive segmentation of 3D data. J. Struct. Biol. *120*, 266–275.

Lindahl, M., Svensson, L.A., Liljas, A., Sedelnikova, S.E., Eliseikina, I.A., Fomenkova, N.P., Nevskaya, N., Nikonov, S.V., Garber, M.B., Muranova, T.A. (1994). Crystal structure of the ribosomal protein S6 from *Thermus thermophilus*. EMBO J. *13*, 1249–1254.

Lodmell, J.S., and Dahlberg, A.E. (1997). A conformational switch in *Escherichia coli* 16S ribosomal RNA during decoding of messenger RNA. Science *277*, 1262–1267.

Malhotra, A., Penczek, P., Agrawal, R.K., Gabashvili, I.S., Grassucci, R.A., Jünemann, R., Burkhardt, N., Nierhaus, K.H., and Frank, J. (1998). *Escherichia coli* 70 S ribosome at 15 Å resolution by cryo-electron microscopy: localization of fMet-tRNA$_f^{Met}$ and fitting of L1 protein. J. Mol. Biol. *280*, 103–116.

Müller, F., and Brimacombe, R. (1997). A new model for the three-dimensional folding of *Escherichia coli* 16S ribosomal RNA. I. Fitting the RNA to a 3D electron microscopic map at 20Å. J. Mol. Biol. *271*, 524–544.

Nikonov, S., Nevskaya, N., Nliseikina, I., Fomenkova, N., Nikulin, A., Ossina, N., Garber, M., Jonsson, B.H., Briand, C., al-Karadaghi, S., et al. (1996). Crystal structure of the RNA binding ribosomal protein L1 from *Thermus thermophilus*. EMBO J. *15*, 1350–1359.

Orlova, E.V., Dube, P., Harris, J.R., Beckman, E., Zemlin, F., Markl, J., and van Heel, M. (1997). Structure of keyhole limpet hemocyanin type 1 (KLH1) at 15 Å resolution by electron cryomicroscopy and angular reconstitution. J. Mol. Biol. *271*, 417–437.

Osswald, M., Greuer, B., and Brimacombe, R. (1990). Localization of a series of RNA-protein cross-link sites in the 23S and 5S ribosomal RNA from *Escherichia coli*, induced by treatment of 50S subunits with three different bifunctional reagents. Nucleic Acids Res. *18*, 6755–6760.

Osswald, M., Doring, T., and Brimacombe, R. (1995). The ribosomal neighbourhood of the central fold of tRNA: cross-links from position 47 of tRNA located at the A, P or E site. Nucleic Acids Res. *23*, 4635–4641.

Peltz, S.W., Hammell, A.B., Cui, Y., Yasenchak, J., Puljanowski, L., and Dinman, J.D. (1999). Ribosomal protein L3 mutants alter translational fidelity and promote rapid loss of the yeast killer virus. Mol. Cell. Biol. *19*, 384–391.

Penczek, P.A., Grassucci, R.A., and Frank, J. (1994). The ribosome at improved resolution: new techniques for merging and orientation refinement in 3D cryo-electron microscopy of biological particles. Ultramicroscopy *53*, 251–270.

Penczek, P., Ban, N., Grassucci, R, Agrawal, R.K., and Frank, J. (1999). *Haloarcula marismortui* 50S subunit—complementarity of EM and X-ray crystallographic information. J. Struct. Biol. *128*, 44–50.

Ramakrishnan, V., and White, S.W. (1992). The structure of ribosomal protein S5 reveals sites of interaction with 16S rRNA. Nature *358*, 768–771.

Schlünzen, F., Kolln, I., Janell, D., Gluhmann, M., Levin, I., Bashan, A., Harms, J., Bartels, H., Auerbach, T., Pioletti, M., et al. (1999). The identification of selected components in electron density maps of prokaryotic ribosomes at 7 angstrom resolution. J. Synchrotron Radiat. *6*, 928–941.

Schmitt, E., Panvert, M., Blanquet, S., and Mechulam, Y. (1998). Crystal structure of methionyl-$tRNA_f^{Met}$ transformylase complexed with the initiator formylmethionyl-$tRNA_f^{Met}$. EMBO J. *17*, 6819–6826.

Spahn, C.M.T., Grassucci, R.A., Penczek, P., and Frank, J. (1999). Direct three-dimensional localization and positive identification of RNA helices within the ribosome by means of genetic tagging and cryo-electron microscopy. Structure *7*, 1567–1573.

Stark, H., Müller, F., Orlova, E.V., Schatz, M., Dube, P., Erdemir, T., Zemlin, F., Brimacombe, R., and van Heel, M. (1995). The 70S *Escherichia coli* ribosome at 23 Å resolution: fitting the ribosomal RNA. Structure *3*, 815–821.

Stark, H., Orlova, E.V., Rinke-Appel, J., Junke, N., Müller, F., Rodnina, M., Wintermeyer, W., Brimacombe, R., and van Heel, M. (1997a). Arrangement of tRNAs in pre- and posttranslocational ribosomes revealed by electron cryomicroscopy. Cell *88*, 19–28.

Stark, H., Rodnina, M.V., Rinke-Appel, J., Brimacombe, R., Wintermeyer, W., and van Heel, M. (1997b). Visualization of elongation factor Tu on the *Escherichia coli* ribosome. Nature *389*, 403–406.

Svergun, D.I., Semenyuk, A.V., and Feigin, L.A. (1988). Small-angle scattering data treatment by the regularization method. Acta Crystallogr. *A44*, 244–250.

van Heel, M. (1986). Noise-limited three-dimensional reconstructions. Optik *73*, 83–86.

Wilson, K.S., and Noller, H.F. (1998). Mapping the position of translational elongation factor EF-G in the ribosome by directed hydroxyl radical probing. Cell *92*, 131–139.

Wimberly, B.T., White, S.W., and Ramakrishnan, V. (1997). The structure of ribosomal protein s7 at 1.9-angstrom resolution reveals a beta-hairpin motif that binds double-stranded nucleic acids. Structure *5*, 1187–1198.

Wimberly, B.T., Guymon, R., McCutcheon, J.P., White, S.W., and Ramakrishnan, V.R. (1999). A detailed view of a ribosomal active site: the structure of the L11-RNA complex. Cell *97*, 491–502.

Wittmann, H.G., Mussig, J., Piefke, J., Gewitz, H.S., Rheinberger, H.J., and Yonath, A. (1982). Crystallization of *Escherichia coli* ribosomes. FEBS Lett. *146*, 217–220.

Wittmann-Liebold, B., Uhlein, M., Urlaub, H., Müller, E.C., Otto, A., and Bischoff, F.R. (1995). Structural and functional implications in the eubacterial ribosome as revealed by protein-rRNA and antibiotic contact sites. Biochem. Cell Biol. *73*, 1187–1197.

Zhu, J., Penczek, P.A., Schröder, R., and Frank, J. (1997). Three-dimensional reconstruction with contrast transfer function correction from energy-filtered cryoelectron micrographs: procedure and application to the 70S *Escherichia coli* ribosome. J. Struct. Biol. *118*, 197–219.

Protein Data Bank ID Code

Coordinates of all ribosomal proteins (C-α backbones) and RNA fragments (P atoms) displayed in the figures have been deposited in the Protein Data Bank (ID code 1EG0), along with the fMet-$tRNA_f^{Met}$ (Schmitt et al., 1998) that was fitted into the cryo-EM density.